DOI: 10.1142/S0218396X1250018X

INTERNATIONAL ASSOCIATION
FOR MATHEMATICS AND
COMPUTERS IN SIMULATION

THREE-DIMENSIONAL SOUND PROPAGATION MODELS USING THE PARABOLIC-EQUATION APPROXIMATION AND THE SPLIT-STEP FOURIER METHOD

YING-TSONG LIN*, TIMOTHY F. DUDA† and ARTHUR E. NEWHALL‡

Applied Ocean Physics and Engineering Department
Woods Hole Oceanographic Institution, Woods Hole, 02543, USA
**ytlin@whoi.edu*
†*tduda@whoi.edu*
‡*anewhall@whoi.edu*

Received 20 January 2012
Accepted 11 May 2012
Published 12 October 2012

The split-step Fourier method is used in three-dimensional parabolic-equation (PE) models to compute underwater sound propagation in one direction (i.e. forward). The method is implemented in both Cartesian (x, y, z) and cylindrical (r, θ, z) coordinate systems, with forward defined as along x and radial coordinate r, respectively. The Cartesian model has uniform resolution throughout the domain, and has errors that increase with azimuthal angle from the x axis. The cylindrical model has consistent validity in each azimuthal direction, but a fixed cylindrical grid of radials cannot produce uniform resolution. Two different methods to achieve more uniform resolution in the cylindrical PE model are presented. One of the methods is to increase the grid points in azimuth, as a function of r, according to nonaliased sampling theory. The other is to make use of a fixed arc-length grid. In addition, a point-source starter is derived for the three-dimensional Cartesian PE model. Results from idealized seamount and slope calculations are shown to compare and verify the performance of the three methods.

Keywords: Split-step Fourier algorithm; underwater sound propagation; 3-D PE.

1. Introduction

Many physical oceanographic and marine geological features can cause significant horizontal reflection and refraction of underwater propagating sound. In many cases, three-dimensional (3-D) models are required for accurately predicting the sound pressure field. A variety of 3-D modeling techniques has been developed over the past decades, and the readers are referred to a review article by Tolstoy[1] for a summary of different modeling techniques. In this paper, we will present one technique using the parabolic equation (PE) approximation, which was originally introduced by Tappert[2] in the 1970's for two-dimensional (2-D) acoustic models. This PE modeling technique is possibly the most efficient and effective model for long-range sound propagation in the ocean.

The parabolic wave equation is derived from the Helmholtz wave equation by considering only one-way out-going waves. The split-step Fourier method was first suggested by Tappert[2] in 1974 for solving this equation. Historically, this method was proposed initially by Tappert[3] to solve the nonlinear Korteweg-de Vries (KdV) wave equation with constant coefficients in the summer of 1972. Later, Hardin and Tappert[4] presented a further application of this method to the solution of nonlinear and variable coefficient wave equations in the fall of 1972. Since the parabolic acoustic wave equation is a variable coefficient wave equation, the split-step Fourier method is readily applicable, and Tappert[2] showed that it is accurate and unconditionally stable. Tappert's early work on PE modeling was summarized in Ref. 5. Note that other approaches are available to solve the parabolic acoustic wave equation: finite difference[6] methods, finite element[7] methods, and split-step Padé[8] solutions. Analysis of these approaches is beyond the scope of this paper, and the readers are referred to Ref. 9 for information on them.

Three-dimensional application of the PE model has also been established. Earlier implementations of the split-step Fourier method can be found in Refs. 10–12 using Cartesian coordinates and in Refs. 13–16 using cylindrical coordinates. Selection between these two approaches depends on the sound field that is considered. For a cylindrical wave-like field the cylindrical model is more suitable, and for a plane wave-like field the Cartesian model is advantageous. The PE approximation errors in these two types of models are different. The forward marching algorithm of the Cartesian PE model is carried out along a single direction, and its approximation error varies in azimuth. On the other hand, the cylindrical PE model remains a consistent approximation along each azimuth because the solutions march out radially. Another difference between these two types of models is the nature of the grid resolution. Fixed-grid Cartesian models have uniform cross-range resolution throughout the domain, but conventional cylindrical models with a fixed azimuth grid suffer from degradation of resolution in the far field. Numerical improvements for cylindrical models to achieve consistent resolution throughout the domain are described in this paper.

Mathematical analyzes of PE model accuracies in different coordinate systems are made here in order to quantify the required grid sizes. Numerical examples of idealized seamount and slope problems are presented. The idealized seamount is axisymmetric. Thus, a sound source placed right above the seamount tip will produce an axisymmetric 2-D sound field, termed an $\mathrm{N} \times 2\mathrm{D}$ field. This provides a good benchmark to test the azimuthal angle validity of the 3-D Cartesian PE model. A source placed away from the tip produces a sound field that is not axisymmetric and provides a scenario for testing the 3-D cylindrical PE model for problems related to irregular resolution. Both the 3-D Cartesian and cylindrical PE models will also be applied to an idealized slope problem and compared to Deane and Buckingham's model[17] that uses the method of images.

This paper extends the work reported in the 10th International Conference on Theoretical and Computational Acoustics held in Taipei, Taiwan in 2011,[18] and it is organized as follows. The theoretical aspect of the 3-D PE modeling technique is first reviewed in Sec. 2, along with a derivation of a wide-angle PE starter for 3-D Cartesian models. Numerical implementations of the 3-D PE theory are explained in Sec. 3, and improvements on the

cylindrical model grid for consistent resolution are shown. Numerical examples are presented in Sec. 4, and the work is summarized in Sec. 5.

2. Theory

The 3-D PE theory is reviewed in this section for model implementations in both Cartesian and cylindrical coordinate systems. Some details are omitted, but the readers will be referred to the literature for further information.

We begin with the linear Helmholtz wave equation for waves of frequency ω, i.e. $p(\mathbf{x}, t) = p(\mathbf{x}) \exp(-i\omega t)$,

$$\boldsymbol{\nabla}^2 p + k_0^2 n^2 p = 0, \tag{1}$$

where $k_0 = \omega/c_0$ is the reference wavenumber, c_0 is the reference sound speed, and n is the index of refraction defined using the reference wavenumber, i.e. $n = c_0/c = k/k_0$. The readers are referred to Pierce and Lee[19] for the influence of the reference wavenumber on the performance of PE models. The index of refraction n is a spatial function. When considering a medium with inhomogeneous density, i.e. the typical acoustic waveguide environment including the seabed in the ocean, one can use a density-reduced pressure variable[20] $\tilde{p} = p/\sqrt{\rho}$, where ρ is the medium density, and reach a wave equation in the same form as Eq. (1):

$$\boldsymbol{\nabla}^2 \tilde{p} + k_0^2 \tilde{n}^2 \tilde{p} = 0, \tag{2}$$

where $\tilde{n}$ is the effective index of refraction,

$$\tilde{n}^2 = n^2 + \frac{1}{2k_0^2}\left[\frac{1}{\rho}\nabla^2\rho - \frac{3}{2\rho^2}(\nabla\rho)^2\right]. \tag{3}$$

This approach of density-reduced pressure was used by Tappert[5] to incorporate water/bottom or sub-bottom interfaces in the PE models. It allows use of the split-step Fourier method, but requires interface smoothing,[8] which may cause some model errors. Note that the anomaly of $\tilde{n}$ depends on the sound frequency and the gradient of the density profile, and for higher frequency and smoothed interfaces the anomaly can be small. Further discussion on this issue will be provided later in the paper. Other approaches were also proposed using, for examples, the finite difference method (see Ref. 21) and the impedance-reduced pressure variable (see Ref. 22). Since they cannot be implemented with the split-step Fourier method, they are not discussed here.

2.1. *PE approximation*

By applying the method of separation of variables and considering only forward propagating sound, we can approximate Eq. (1) or (2) by a parabolic-type partial differential equation. A brief derivation is shown here to explain this approximation.

For the two coordinate systems, the sound pressure is first decomposed into the following expressions:

$$\begin{cases} p(x,y,z) = \varphi(y,z,x)\exp(ik_0 x) & \text{in Cartesian coordinates,} \\ p(r,\theta,z) = r^{-1/2}\varphi(\theta,z,r)\exp(ik_0 r) & \text{in cylindrical coordinates,} \end{cases} \tag{4}$$

where the reduced variable φ is essentially the demodulated pressure with the baseline phase removed according to the reference wavenumber k_0. In the cylindrical coordinate system, the geometric spreading loss $r^{-1/2}$ is also removed. A unified formula for determining the outgoing demodulated pressure φ in both coordinate systems can be written as[5]

$$\frac{\partial}{\partial\eta}\varphi(\mathbf{x}_\perp,\eta) = ik_0\left\{-1+\sqrt{k_0^{-2}\boldsymbol{\nabla}_\perp^2 + n^2(\mathbf{x}_\perp,\eta)}\right\}\varphi(\mathbf{x}_\perp,\eta), \tag{5}$$

where $\mathbf{x}_\perp$ denotes the transverse coordinates, $\mathbf{x}_\perp = (y,z)$ or (θ,z), and η denotes position in the marching direction of the solution, i.e. along the x-axis in Cartesian models or along the radial axis r in cylindrical models. The 2-D Laplacian $\boldsymbol{\nabla}_\perp^2$ denotes the following partial differential operators:

$$\begin{cases} \boldsymbol{\nabla}_\perp^2 = \dfrac{\partial^2}{\partial y^2} + \dfrac{\partial^2}{\partial z^2} & \text{in Cartesian coordinates,} \\ \boldsymbol{\nabla}_\perp^2 = \dfrac{1}{r^2}\dfrac{\partial^2}{\partial\theta^2} + \dfrac{\partial^2}{\partial z^2} & \text{in cylindrical coordinates.} \end{cases} \tag{6}$$

Equation (5) is a nonlinear parabolic partial differential equation because of the square-root operator. Tappert[2] applied the following rational linear approximation to the square-root operator and reduced Eq. (5) to a linear parabolic equation.

$$\sqrt{k_0^{-2}\boldsymbol{\nabla}_\perp^2 + n^2(\mathbf{x}_\perp,\eta)} \cong (k_0^{-2}\boldsymbol{\nabla}_\perp^2 + n^2(\mathbf{x}_\perp,\eta) + 1)/2. \tag{7}$$

An error analysis with the normal mode approach proposed by McDaniel[23] suggested that Tappert's approximation yields an acceptable phase error of 0.0002 to a region of $\pm 10^\circ$ around the PE marching direction.[9] Another approximation form was proposed by Feit and Fleck,[10]

$$\sqrt{k_0^{-2}\boldsymbol{\nabla}_\perp^2 + n^2(\mathbf{x}_\perp,\eta)} \cong \sqrt{k_0^{-2}\boldsymbol{\nabla}_\perp^2 + 1} + n(\mathbf{x}_\perp,\eta) - 1, \tag{8}$$

and this approximation was first used by Thomson and Chapman[24] for a wide angle 2-D PE model in underwater acoustics. Implementations with 3-D Cartesian coordinates were made by Feit and Fleck[10] in optics, by Duda[12] in underwater acoustics, and by Huang and Fehler[25] in seismology. Although this improved approximation will yield a nonlinear parabolic equation, the split-step Fourier method is still applicable. The details are explained in the next section. Here, we will first discuss the PE approximation error.

One can take McDaniel's normal mode approach[23] to analyze the phase error of any rational linear PE approximation. However, the normal mode approach is not applicable to

the nonlinear approximation, because the resultant PE modes are no longer the Helmholtz modes (see Ref. 26 for detailed discussion). Here we follow Feit and Fleck[10] to analyze the approximation along the PE marching direction by examining its error defined as

$$\mathbf{E} = ((k_0^{-2}\boldsymbol{\nabla}_\perp^2 + 1)^{1/2} + n - 1)^2 - (k_0^{-2}\boldsymbol{\nabla}_\perp^2 + n^2).$$

This error analysis was also used by Thomson and Chapman[24] in their 2-D wide-angle PE model. Note that when $n = 1$, Feit and Fleck's approximation recovers the original square-root operator, and $\mathbf{E} = 0$.

Consider 3-D sound waves with a single wavenumber component, say, $p = \exp(i\mathbf{k}\cdot\mathbf{x})$, and let the angle between the wavenumber vector $\mathbf{k}$ and the PE marching direction to be γ. The error bound of the approximation is shown by Thomson and Chapman[24] to be dependent on the angle γ and the anomaly δn of the refraction index:

$$|\mathbf{E}(\delta n, \gamma)| \leq 2|\delta n||\cos\gamma - 1|. \tag{9}$$

With the same approach Thomson and Chapman[24] also found the error bound for Tappert's standard approximation equal to $[|\delta n|(2 + |\delta n|) + \sin^2\gamma]^2/4$. The error bounds of these two PE approximations are plotted in Fig. 1 as a function of $|\delta n|$ and γ, and it shows that Feit and Fleck's approximation achieves better accuracy and provides a wider valid angle measured from the PE marching direction.

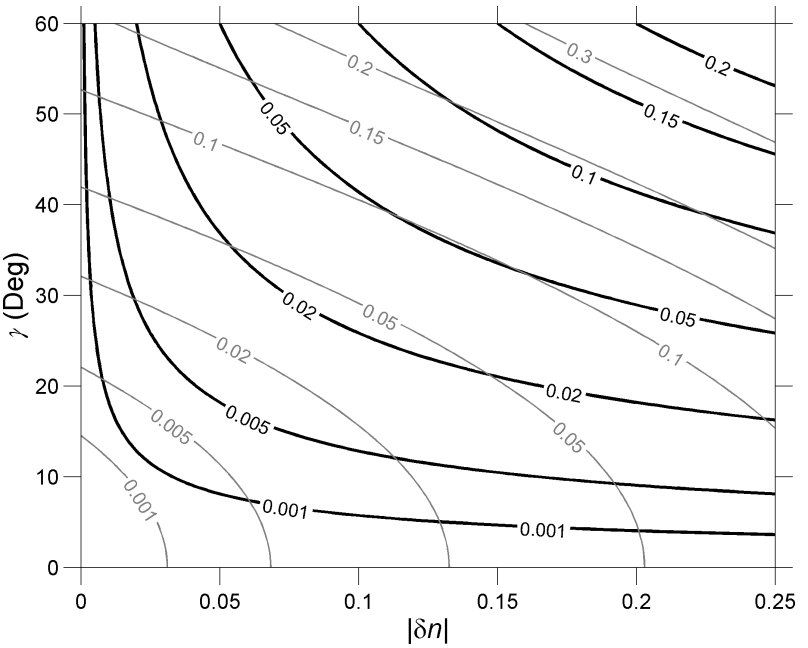

Fig. 1. Error bounds of two different PE approximations that can be used with the split-step Fourier method. The dark contours are the error bounds of Feit and Fleck's radical approximation, and the light contours are the error bounds of Tappert's standard rational approximation.

2.2. *Split-step Fourier method*

We will employ a numerical scheme with first-order accuracy in the marching step size $\Delta\eta$ to explain the split-step Fourier method, and a second-order scheme will be provided later in this section. Substituting the square root operator in Eq. (5) with the wide-angle approximation yields

$$\frac{\partial}{\partial\eta}\varphi(\mathbf{x}_\perp,\eta) = ik_0\big[-1+\sqrt{k_0^{-2}\boldsymbol{\nabla}_\perp^2+1}+n(\mathbf{x}_\perp,\eta)-1\big]\varphi(\mathbf{x}_\perp,\eta). \tag{10}$$

The formal solution of Eq. (10) with first-order accuracy can be found from a split-step formula:

$$\varphi(\mathbf{x}_\perp,\eta+\Delta\eta) = e^{ik_0\Delta\eta[n(\mathbf{x}_\perp,\eta)-1]}e^{ik_0\Delta\eta[-1+\sqrt{k_0^{-2}\boldsymbol{\nabla}_\perp^2+1}]}\varphi(\mathbf{x}_\perp,\eta), \tag{11}$$

where the first exponential operator handles refraction due to the medium inhomogeneity, and the second one handles free propagation with the reference wavenumber k_0. The Fourier transform is utilized to implement the free propagation operator[2–5] in the wavenumber domain, i.e.

$$\mathrm{e}^{ik_0\Delta\eta[-1+\sqrt{k_0^{-2}\boldsymbol{\nabla}_\perp^2+1}]}\varphi(\mathbf{x}_\perp,\eta) = \mathcal{F}^{-1}\{\mathrm{e}^{i\Delta\eta[-k_0+\sqrt{k_0^2-|\mathbf{k}_\perp|^2}]}\mathcal{F}\{\varphi(\mathbf{x}_\perp,\eta)\}\}, \tag{12}$$

where $k_\perp$ indicates the transverse component of the reference wavenumber vector, i.e. $|\mathbf{k}_\perp| = (k_y^2+k_z^2)^{1/2}$ in the Cartesian PE model, and $|\mathbf{k}_\perp| = (r^{-2}k_\theta^2+k_z^2)^{1/2}$ in the cylindrical PE model. The Fourier transform pair in each coordinate system is listed below.

$$\begin{cases} F(k_y,k_z) = \mathcal{F}\{f(y,z)\} = \displaystyle\int_{\mathbb{R}^2} f(y,z)\mathrm{e}^{-i(k_y y+k_z z)}dydz, \\ f(y,z) = \mathcal{F}^{-1}\{F(k_y,k_z)\} = \dfrac{1}{(2\pi)^2}\displaystyle\int_{\mathbb{R}^2} F(k_y,k_z)\mathrm{e}^{i(k_y y+k_z z)}dk_y dk_z, \end{cases} \tag{13.1}$$

$$\begin{cases} F(k_\theta,k_z) = \mathcal{F}\{f(\theta,z)\} = \displaystyle\int_{\mathbb{R}^2} f(\theta,z)\mathrm{e}^{-i(k_\theta\theta+k_z z)}rd\theta dz, \\ f(\theta,z) = \mathcal{F}^{-1}\{F(k_\theta,k_z)\} = \dfrac{1}{(2\pi)^2}\displaystyle\int_{\mathbb{R}^2} F(k_\theta,k_z)\mathrm{e}^{i(k_\theta\theta+k_z z)}r^{-1}dk_\theta dk_z. \end{cases} \tag{13.2}$$

Substituting the free propagation operator into Eq. (11) with its Fourier transform yields

$$\Phi(\mathbf{k}_\perp,\eta+\Delta\eta) = \mathcal{F}\{\mathbf{B}(\mathbf{x}_\perp,\eta)\mathcal{F}^{-1}\{\mathbf{Q}(\mathbf{k}_\perp,\eta)\Phi(\mathbf{k}_\perp,\eta)\}\}, \tag{14}$$

where Φ is the wavenumber spectrum of φ, i.e. $\Phi(\mathbf{k}_\perp,\eta) = \mathcal{F}\{\varphi(\mathbf{x}_\perp,\eta)\}$, $\mathbf{B}$ is the phase screen of refraction applied in the spatial domain, and $\mathbf{Q}$ is the free propagation operator from η to $\eta+\Delta\eta$ with the phase advance $\Delta\eta\times\sqrt{k_0^2-|\mathbf{k}_\perp|^2}$. The detailed formulations of

operators $\mathbf{B}$ and $\mathbf{Q}$ are

$$\mathbf{B}(\mathbf{x}_\perp, \eta) = \mathrm{e}^{ik_0 \Delta\eta [n(\mathbf{x}_\perp, \eta) - 1]} \quad \text{and} \tag{15}$$

$$\mathbf{Q}(\mathbf{k}_\perp, \eta) = \mathrm{e}^{i\Delta\eta [-k_0 + \sqrt{k_0^2 - |\mathbf{k}_\perp|^2}]}. \tag{16}$$

Note that the exponent $-i\Delta\eta k_0$ in the free propagation operator $\mathbf{Q}$ is due to the fact that the variable $\varphi(\mathbf{x}_\perp, \eta)$ is the demodulated pressure with the baseline phase removed according to the reference wavenumber k_0 (see Eq. (4)).

Equation (14) is the split-step Fourier PE solution with first-order accuracy, and one complete marching step of the PE solution from η to $\eta + \Delta\eta$ is split into two steps: the free propagation step with $\mathbf{Q}$ and the refraction step with $\mathbf{B}$. The solution with second-order accuracy can be found by considering half-step operators,

$$\begin{aligned} &\mathbf{B}_{\frac{1}{2}}^{-1}(\mathbf{x}_\perp, \eta + \Delta\eta) \mathcal{F}^{-1}\{\mathbf{Q}_{\frac{1}{2}}^{-1}(\mathbf{k}_\perp, \eta + \Delta\eta) \Phi(\mathbf{k}_\perp, \eta + \Delta\eta)\} \\ &\quad = \varphi\left(\mathbf{x}_\perp, \eta + \frac{\Delta\eta}{2}\right) \\ &\quad = \mathbf{B}_{\frac{1}{2}}(\mathbf{x}_\perp, \eta) \mathcal{F}^{-1}\{\mathbf{Q}_{\frac{1}{2}}(\mathbf{k}_\perp, \eta) \Phi(\mathbf{k}_\perp, \eta)\}, \end{aligned} \tag{17}$$

where

$$\mathbf{B}_{\frac{1}{2}}(\mathbf{x}_\perp, \eta) = \mathrm{e}^{ik_0 \frac{\Delta\eta}{2} [n(\mathbf{x}_\perp, \eta) - 1]} \quad \text{and} \tag{18}$$

$$\mathbf{Q}_{\frac{1}{2}}(\mathbf{k}_\perp, \eta) = \mathrm{e}^{i\frac{\Delta\eta}{2} [-k_0 + \sqrt{k_0^2 - |\mathbf{k}_\perp|^2}]}. \tag{19}$$

The right-hand side of Eq. (17) represents forward marching from η to $\eta + \Delta\eta/2$, and its left-hand side is due to the second half-step marching from $\eta + \Delta\eta/2$ to $\eta + \Delta\eta$, written as an inverse operator. By applying the operator $\mathbf{B}_{\frac{1}{2}}(\mathbf{x}_\perp, \eta + \Delta\eta)$ to each side of Eq. (17), and using the approximation $[\mathbf{B}_{\frac{1}{2}}(\mathbf{x}_\perp, \eta + \Delta\eta) \cdot \mathbf{B}_{\frac{1}{2}}(\mathbf{x}_\perp, \eta)] \cong \mathbf{B}(\mathbf{x}_\perp, \eta + \frac{1}{2}\Delta\eta)$, one obtains a split-step solution with second-order accuracy:

$$\Phi(\mathbf{k}_\perp, \eta + \Delta\eta) = \mathbf{Q}_{\frac{1}{2}}(\mathbf{k}_\perp, \eta + \Delta\eta) \mathcal{F}\left\{\mathbf{B}\left(\mathbf{x}_\perp, \eta + \frac{1}{2}\Delta\eta\right) \mathcal{F}^{-1}\{\mathbf{Q}_{\frac{1}{2}}(\boldsymbol{k}_\perp, \eta) \Phi(\mathbf{k}_\perp, \eta)\}\right\}. \tag{20}$$

2.3. *3-D point-source starter*

The PE model needs an initial starter at range equal to 0 to simulate a sound source, and many approaches have been introduced.[9] In this paper, we will use the wavenumber spectral approach introduced by Thomson and Bohun[27] to make a point source starter for the 3-D Cartesian PE model.

Thomson and Bohun's approach[27] was originally introduced for the 2-D cylindrical PE model. It makes use of the wavenumber spectrum of an axisymmetric sound field bounded by a pressure-release boundary and with a point source placed at depth z_0 below it. The pressure-release boundary is employed for simulating the sea surface, and in a cylindrical

coordinate system the wavenumber spectrum of the axisymmetric sound field at $r = 0$ is shown to be[28]

$$\Phi_0(k_z) = 2\sqrt{2\pi}\mathrm{e}^{-i\frac{\pi}{4}}\frac{\sin(k_z z_0)}{(k_0^2 - k_z^2)^{1/4}}. \tag{21}$$

The inverse Fourier transform of Eq. (21) at $z > 0$ is the sound field in the water (the image field being at $z < 0$), and it can be taken as the initial spectrum of a 3-D cylindrical PE starter in each azimuth.

To apply the wavenumber approach to the 3-D Cartesian PE model, we first consider the Helmholtz wave equation with a given reference wavenumber k_0 and a point source at $x = 0$, $y = y_0$ and $z = z_0$ (using the Dirac delta function):

$$\boldsymbol{\nabla}^2 p + k_0^2 p = -4\pi\delta(x)\delta(y - y_0)\delta(z - z_0). \tag{22}$$

Applying the 2-D Fourier transform, Eq. (13.1), on the both sides of Eq. (22), we obtain the governing equation for the wavenumber spectrum $P(k_y, k_z, x)$,

$$\frac{d^2}{dx^2}P + (k_0^2 - k_y^2 - k_z^2)P = -4\pi\mathrm{e}^{-i(k_y y_0 + k_z z_0)}\delta(x), \tag{23}$$

which is a standard ordinary differential equation with the solution

$$P(k_y, k_z, x) = \frac{2i\pi}{(k_0^2 - k_y^2 - k_z^2)^{1/2}}\mathrm{e}^{-i(k_y y_0 + k_z z_0)}\mathrm{e}^{ix(k_0^2 - k_y^2 - k_z^2)^{1/2}}. \tag{24}$$

Lastly, we apply the method of images and yield the initial spectrum for a 3-D Cartesian PE starter at $x = 0$,

$$\Phi_0(k_y, k_z) = 4\pi\frac{\sin(k_z z_0)}{(k_0^2 - k_y^2 - k_z^2)^{1/2}}\mathrm{e}^{-ik_y y_0}. \tag{25}$$

3. Numerical Implementation

Implementation of the split-step Fourier PE model requires numerical computations of discrete Fourier transforms, and the Nyquist sampling theorem shows that the discrete spatial and wavenumber domains are connected in the following way.

$$k_\mu^{\max} = \pi/\Delta\mu, \quad \Delta k_\mu = \pi/L_\mu \quad (-L_\mu \le \mu \le L_\mu, -k_\mu^{\max} \le k_\mu \le k_\mu^{\max}), \tag{26}$$

where μ indicates the transverse coordinates of either y, z, or θ. The spatial aperture is $2L_\mu$, and the wavenumber aperture is $2k_\mu^{\max}$. These relations are fundamental and can be used to derive the requirement for the model grid sizes.

Numerical implementation of the PE model also involves imitating the radiation boundary condition. There are several ways to do so, including the perfectly matched layer approach,[29] the artificial absorption layer approach,[9] etc. The artificial absorption layer approach is taken here. In this method, the field is multiplied by a real function equal to one in the usable part of the domain that decreases to near zero at the domain boundary.[9,11]

3.1. *Model grid sizes*

Consider that we want the sound propagation model to sample all of the arrivals at angles less than a given maximum $\gamma_{\max}$, with a required angular resolution $\Delta\gamma_{\min}$. The arrival angle γ is measured from the PE marching direction, i.e. $\hat{e}_x$ in Cartesian models and $\hat{e}_r$ in cylindrical models. From the Nyquist sampling theorem, we can determine the required Δk_μ and $k_\mu^{\max}$ from the geometric relation of the wavenumber components shown in Fig. 2, i.e. $(k_y^2 + k_z^2)^{1/2} = |\mathbf{k}| \sin\zeta$, and $(k_\theta^2/r^2 + k_z^2)^{1/2} = |\mathbf{k}| \sin\xi$.

The free propagation step in the split-step Fourier PE model can be considered as sound propagating in a field with the constant reference wavenumber k_0. To sample all of the arrivals less than the given angle $\gamma_{\max}$, the maximum k_μ must satisfy the following condition:

$$k_{y,z}^{\max} \geq k_0 \sin\gamma_{\max} \quad \text{and} \quad k_\theta^{\max} \geq k_0 r \sin\gamma_{\max}, \tag{27.1}$$

or equivalently for Δy, Δz, and $\Delta\theta$,

$$\Delta y, \Delta z \leq (\sin\gamma_{\max})^{-1}\lambda_0/2 \quad \text{and} \quad \Delta\theta \leq (r\sin\gamma_{\max})^{-1}\lambda_0/2. \tag{27.2}$$

It can also be shown that the interval between resolved arrival angles $\Delta\gamma$ is equal to $k_0^{-1}\sec\gamma\Delta k_{y,z}$ in Cartesian coordinates, or $r^{-1}(k_0^{-1}\sec\gamma\Delta k_\theta - \tan\gamma\Delta r)$ in cylindrical coordinates. Therefore, to achieve a given angular resolution $\Delta\gamma_{\min}$, the wavenumber increment

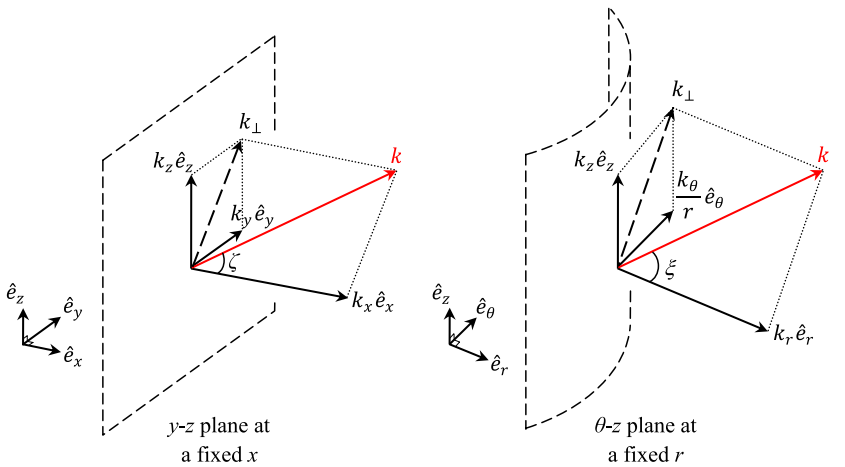

(a) Wavenumber domain (b) Spatial domain

Fig. 2. Wavenumber decomposition in (a) Cartesian and (b) cylindrical coordinate systems. A given wavenumber vector $\mathbf{k}$ is expressed in Cartesian coordinates as $\mathbf{k} = k_x\hat{e}_x + k_y\hat{e}_y + k_z\hat{e}_z$, where $k_x = |\mathbf{k}|\cos\zeta$, and $(k_y^2 + k_z^2)^{1/2} = |\mathbf{k}|\sin\zeta$. On the other hand, the same wavenumber vector is expressed in cylindrical coordinates as $\mathbf{k} = k_r\,\hat{e}r + k_\theta/r\hat{e}_\theta + k_z\hat{e}_z$, where $k_r = |\mathbf{k}|\cos\xi$, and $(k_\theta^2/r^2 + k_z^2)^{1/2} = |\mathbf{k}|\sin\xi$. The angles ζ and ξ are measured from the unit vectors $\hat{e}_x$ and $\hat{e}_r$, respectively. Since $\hat{e}_x$ and $\hat{e}_r$ are not always in the same direction, ζ and ξ can be different.

$\Delta k_{y,z,\theta}$ has to satisfy the conditions

$$\Delta k_{y,z} \le k_0 \cos\gamma \Delta\gamma_{\min}, \quad \text{and} \quad \Delta k_\theta \le k_0(r\cos\gamma\Delta\gamma_{\min} + \sin\gamma\Delta r), \tag{28.1}$$

or equivalently for L_y, L_z and L_θ,

$$L_{y,z} \ge (\cos\gamma\Delta\gamma_{\min})^{-1}\lambda_0/2 \quad \text{and} \quad L_\theta \ge (r\cos\gamma\Delta\gamma_{\min} + \sin\gamma\Delta r)^{-1}\lambda_0/2. \tag{28.2}$$

Examination of these conditions reveals that the required $\Delta\theta$ is a function of radial distance, as is the required angular aperture L_θ. For a common marching algorithm used in cylindrical PE models, i.e. marching along each radial in a fixed $\Delta\theta$ grid, the maximal arrival angle that the cylindrical PE model can resolve will gradually decrease as the distance goes further and further, and the horizontal resolution also decreases. One simple way to fix the problem is to make $\Delta\theta$ very small, but this will result in unnecessary oversampling at a shorter distance. New marching algorithms to overcome this numerical issue in the cylindrical PE model are presented in the next section.

3.2. *Model grids and marching algorithms for 3-D cylindrical PE models*

Implementing a PE model in the Cartesian coordinate system is less trouble, because a fixed Cartesian grid can provide uniform resolution throughout the domain. We only need to make sure the grid sizes obey the sampling condition mentioned in the previous section. Two cylindrical model grids and marching algorithms are provided here to overcome the resolution issue. In brief, one method is to apply the upsampling method[30] in digital signal processing to increasing the grid points in azimuth, and the other is to transform the θ coordinate to the arc-length s coordinate.

3.2.1. *Azimuthal grid upsampling*

The simplest implementation of the cylindrical PE marching algorithm uses a fixed *azimuthal* grid. The PE solution $\varphi(\theta, z, r)$ at one range r is then marched to the next range $r + \Delta r$ seamlessly on the fixed (θ, z) grid. However, as shown in the previous section, a fixed θ grid cannot produce a consistent model resolution throughout the calculation domain. This problem can be overcome by implementing the marching algorithm in the wavenumber domain, i.e. to march the wavenumber spectrum of the PE solution $\Phi(k_\theta, k_z, r)$.

Equation (27.1) shows that the required angular wavenumber aperture for resolving a given arrival angle is smaller at a shorter distance (smaller r). When a larger wavenumber aperture is required at a longer distance, we can zero-pad the angular spectrum at both ends, depicted in Fig. 3(a). As long as the tails of the angular spectrum are insignificant, the zero-padding will not produce any artifacts. According to the sampling theorem, this zero-padding procedure will effectively produce a finer angular grid at the next radial step, as shown in Fig. 3(b). This zero-padding procedure is in fact the standard upsampling method[30] in digital signal processing, and it can be done at each marching step or

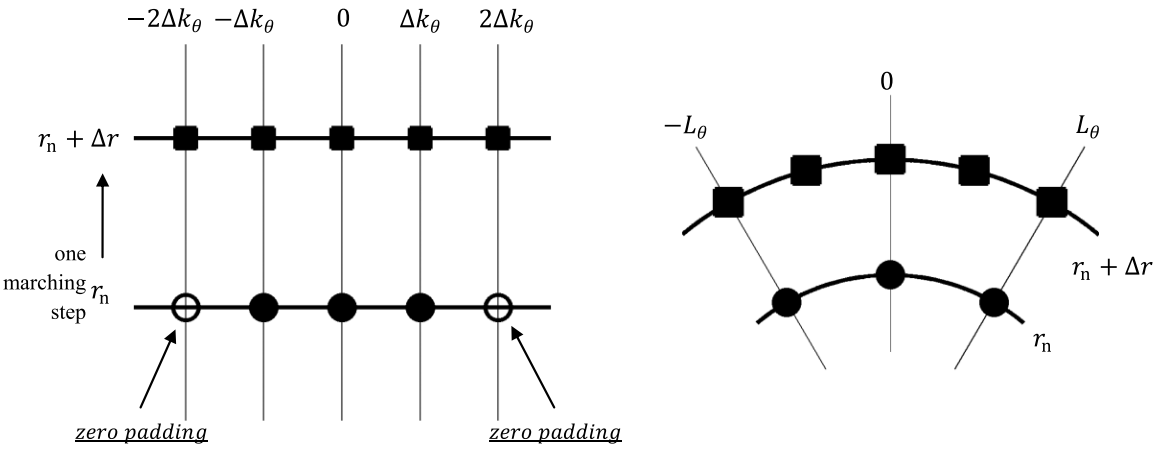

(a) Wavenumber gomain (b) Spatial domain

Fig. 3. θ grid upsampling with zero padding at r_n on the wavenumber spectrum.

intermittently when a larger wavenumber aperture is required. There is no penalty for working on wavenumber spectra in the split-step Fourier PE model because the transforms are already needed. The idea of azimuthal grid upsampling has also been used by Sturm and Kampanis[31] and by Austin and Chapman[32] to increase the model resolution in their cylindrical 3-D PE models.

Since the angular aperture is fixed, this zero-padding technique may still have a problem with arrivals that exceed the angular aperture at a shorter range from the source. A simple solution is to increase the angular aperture, but this becomes inefficient in the far field where the aperture exceeds the model area of interest. The next method using the arc-length s coordinate will not have this issue.

3.2.2. *Arc-length grid*

Another marching algorithm requires a coordinate transformation from the azimuth angle θ to the arc length s, and the resultant grid will have consistent model resolution in the far field. The grid transformation is derived simply from $s = r\theta$, and according to fundamental geometrical algebra it follows that $ds = rd\theta$ and $k_s = k_\theta/r$ at a fixed r. Hence, the Fourier transform pair on (s, z) can be found by changing the variables θ and k_θ in Eq. (13.2), i.e.

$$\begin{cases} F(k_s, k_z) = \mathcal{F}\{f(s,z)\} = \displaystyle\int_{\mathbb{R}^2} f(s,z) e^{-i(k_s s + k_z z)} ds dz, \\ f(s,z) = \mathcal{F}^{-1}\{F(k_s,k_z)\} = \dfrac{1}{(2\pi)^2} \displaystyle\int_{\mathbb{R}^2} F(k_s,k_z) e^{i(k_s s + k_z z)} dk_s dk_z. \end{cases} \tag{29}$$

The discrete sampling relation between s and k_s follows Eq. (26). Thus, the requirements for the s grid follow the same conditions as the Cartesian grid, i.e. $\Delta s \leq (\sin\gamma_{\max})^{-1}\lambda_0/2$ and $L_s \geq (\cos\gamma\Delta\gamma_{\min})^{-1}\lambda_0/2$.

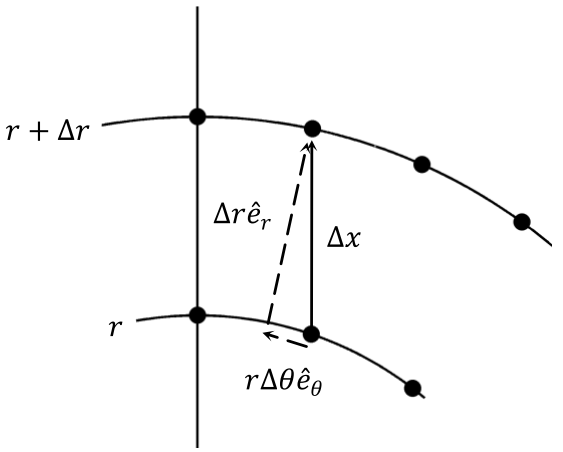

Fig. 4. The path of free propagation in the fixed Δs PE model, where $\Delta\theta = (\frac{s}{r+\Delta r} - \frac{s}{r})$.

The split-step marching algorithm with the arc-length grid is given by

$$\Phi(k_s, k_z, r + \Delta r) = \mathcal{F}\{\mathbf{B}(s, z, r)\mathcal{F}^{-1}\{\mathbf{Q}(k_s, k_z, r)\Phi(k_s, k_z, r)\}\}, \tag{30}$$

where the operator $\mathbf{B}$ is the phase screen defined in Eq. (15), and $\mathbf{Q}$ is the free propagation operator. As shown in Fig. 4, the path of the free propagation from (r, s, z) to $(r + \Delta r, s, z)$ is $\Delta\mathbf{x} = \Delta r\ \hat{e}_r + r\Delta\theta\ \hat{e}_\theta$ with $\Delta\theta = (\frac{s}{r+\Delta r} - \frac{s}{r})$, and so the phase advance due to the free propagation is $\mathbf{k} \cdot \Delta\mathbf{x} = k_r\Delta r + k_\theta\Delta\theta$, where $k_r = \sqrt{k_0^2 - r^{-2}k_\theta^2 - k_z^2}$. This makes the free propagation operator equal to the following exponential function.

$$\mathbf{Q}(k_s, k_z, r) = \mathrm{e}^{-ik_0\Delta r + i(k_r\Delta r + k_\theta\Delta\theta)} = \mathrm{e}^{i\Delta r(-k_0 + \sqrt{k_0^2 - k_s^2 - k_z^2}) + ik_s s(\frac{-\Delta r}{r+\Delta r})}, \tag{31}$$

where the coordinate transformation ($s = r\theta$ and $k_s = k_\theta/r$) is carried out. Combining Eqs. (30) and (31), we can find that the free propagation is implemented as

$$\begin{aligned}&\mathcal{F}^{-1}\{\mathbf{Q}(k_s, k_z, r)\Phi(k_s, k_z, r)\}\\ &\quad = \frac{1}{(2\pi)^2}\int_{\mathbb{R}^2} \Phi(k_s, k_z, r)\mathrm{e}^{i\Delta r(-k_0 + \sqrt{k_0^2 - k_s^2 - k_z^2})}\mathrm{e}^{ik_s s(\frac{r}{r+\Delta r})}\mathrm{e}^{ik_z z}dk_s dk_z.\end{aligned} \tag{32}$$

Besides achieving uniform model resolution in the far field, this fixed-Δs marching algorithm has another attractive feature. Since the arc-length interval Δs and the arc-length aperture L_s are fixed, the equivalent angular aperture (L_s/r) at shorter ranges can extend beyond 360°. Thus, the model grid can cover the entire azimuth many times over in the near field, and it will gradually unwrap as the radius goes further. The sampling of the field will be very good at close range for the following reason. As long as Δr and Δs are rational numbers, the sampling points with angular separation $\Delta s/\Delta r$ will never overlap because π is an irrational number.

Implementation of the fixed-Δs grid for the PE solution with second-order accuracy, Eq. (20), is straightforward. We only need to follow Eq. (19) to use $\mathbf{Q}_{1/2}(k_s, k_z, r)$ for each $\Delta r/2$ free propagation step.

4. Numerical Examples

Applications of the 3-D PE models to idealized seamount and slope problems are presented in this section. The purpose of these numerical examples is to demonstrate the model performance, and also to compare the models implemented in different coordinate systems. A hyperbolic tangent smoothing procedure[5] is used to smooth the discontinuity of density at the seafloor for using the density-reduced pressure variable. This smoothing procedure will produce model errors to the PE solutions. However, since the width of the smoothing kernel is on the order of the acoustic wavelength, the model errors caused by the interface smoothing are smaller for higher frequency (order of a hundred Hz and above). The artificial absorption layer approach[9] is used here to imitate the radiation boundary condition, and the PE solution within the artificial layers will be discarded. The discarded region is 1/8 of the total domain width on each side in y and 1/4 of the total depth in z at the bottom of the model domain, so only $3/4 \times 3/4$ of the total domain area is usable. A stair-step approximation is employed for the sloping bottom in the following PE calculations.

4.1. *Idealized seamount problem*

In this idealized seamount problem we will carry out numerical tests to the split-step Fourier (SSF) PE model. These tests include how well the model handles the range-dependent bathymetry and how wide the valid azimuthal range is in the 3-D Cartesian PE model. We will also demonstrate the improved model grids and marching algorithms for the 3-D cylindrical PE model.

The model parameters of the idealized seamount are explained here. The summit of the seamount is at depth 200 m, and its slope is $1/8 (\sim 7^\circ$ in angle). The radius of the seamount is 2500 m, and the water depth outside the seamount area is 512.5 m. The water column is homogeneous with sound speed 1500 m/s, density 1.0 g/cm^3 and no medium absorption for sound waves. The bottom is also homogenous with sound speed 1700 m/s, density 1.5 g/cm^3 and medium absorption 0.5 dB per wavelength. Two source positions, one above the tip of the seamount and one off the tip, are considered in this example, as shown in Fig. 5.

4.1.1. *Source above the tip of the seamount*

In this first example, a 100-Hz point source is placed right above the summit of the seamount, which is located at the origin of the coordinate system, and the source depth is 100 m. Since the seamount is axisymmetric, the point source will produce an axisymmetric 2-D (N $\times$ 2D) sound field. Thus, we can examine the SSF PE model by comparing with a verified 2-D model. This example provides a benchmark for testing the valid azimuthal range of the 3-D Cartesian SSF PE model.

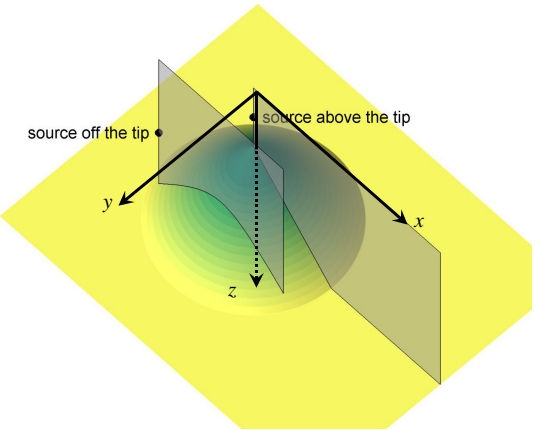

Fig. 5. Geometry of the idealized seamount problem. Two source positions are considered, and the frequency is 100 Hz.

First, the capability of the SSF PE model to handle the range-dependent bathymetry is examined by comparing with an established and well-recognized 2-D PE model using the split-step Padé approximation,[8] named RAM PE. The calculation setup of both PE models is explained below. In the 2-D RAM PE model, the marching step size Δx is 0.5 m (one thirtieth of the acoustic wavelength in the water column), and the depth grid size Δz is 0.125 m. The reference sound speed is 1500 m/s, and the number of Padé coefficients is four. In the SSF PE model, the marching step size Δx is 2 m, the cross-range grid size Δy is 1 m, and the depth grid size Δz is 0.5 m. The reference sound speed is 1495 m/s, and the one-side halfway width of the hyperbolic tangent smoothing for the water/bottom interface is set to be 1 m. The angular aperture of the wide-angle point source starter (see Sec. 2.3) terminates at 84° with a gradual ramp-down from 82.5°.

The convergence of both the SSF and RAM PE models is ensured, and the model comparison is shown in Fig. 6. Transmission loss (TL) on the vertical slide across the source is plotted as contours with a 5 dB increment, and good agreement between the two PE models is observed, see Figs. 6(a) and 6(b). Significant discrepancy is seen at the higher angle near the source, and this is due to the different aperture of the point source starter used in each PE model. Detailed comparison is made for the TL at 100 m depth shown in Fig. 6(c), and the overall difference of the TL is found less than 1 dB. More importantly, the interference patterns match very well, indicating good agreement in the phase of sound pressure. Since the RAM PE has been well tested and verified, we can confirm the accuracy of the SSF PE model in an N × 2D environment with a sloping bottom.

Next, we will examine the valid azimuthal angle of the 3-D Cartesian SSF PE model. In this test, the 3-D cylindrical SSF PE solution is considered to be the reference solution. Since the sound field is N × 2D, its angular gradient diminishes, but the cross-range gradient along y still appears in the Cartesian PE model. Figures 7(a) and 7(b) present the vertical TL contours from both models on the y–z plane at $x = 2$ km. Excellent agreement can be observed in $|y| < 1$ km. Detailed comparison of the TL at $x = 2$ km and $z = 150$ m along y is

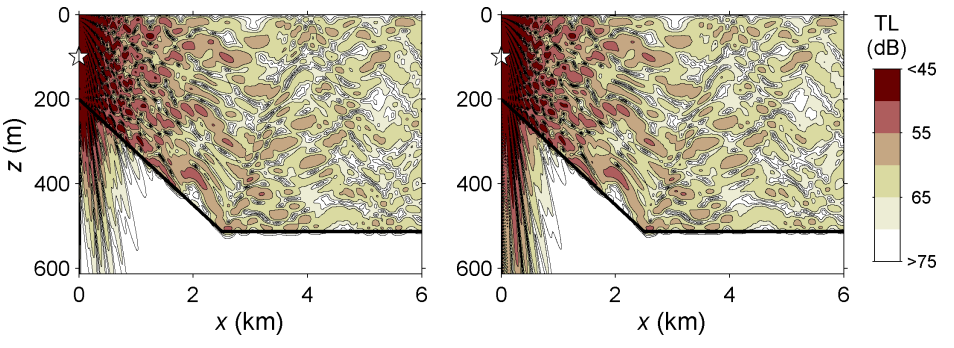

(a) RAM PE solution

(b) SSE PE solution

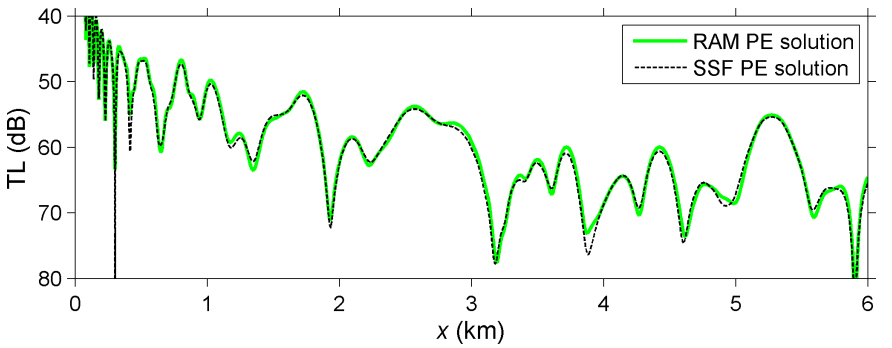

(c) TL at 100 m depth

Fig. 6. Comparison of the TL solutions from two different PE models. The 100-Hz sound source is placed above the tip of the seamount as shown in Fig. 5, and the TL on the x–z plane across the source obtained from both the PE models is plotted in panels (a) and (b), along with the TL at 100 m depth shown in panel (c).

shown in Fig. 7(c), and it confirms that the 3-D Cartesian PE model handles the cross-range variability extremely well within $\pm 20°$ in azimuth.

4.1.2. *Source off the tip of the seamount*

The 100-Hz sound source in this second example is placed away from the tip of the seamount at $x = -2$ km, $y = 850$ m and $z = 250$ m, as depicted in Fig. 5. The sound pressure field is full 3-D due to the out-of-plane reflection of sound from the seamount bathymetry.

Two 3-D cylindrical SSF PE models are implemented with and without the θ grid upsampling which ensures that the size of the angular grid is always smaller than 1 m throughout the domain. When the upsampling is not implemented, the angular interval of the model grid is fixed to 0.016 rad, which is 48 m in length at a radius of 3 km, and the PE model will lose its resolution in the far field. The PE solutions march out in radial with a 2-m step, and the TL solutions on the vertical x–z plane passing the source are shown in Figs. 8(a) and 8(b). The TL values (intensities) calculated from these two models differ clearly at $x > 1$ km (~ 3 km from the source). Detailed comparisons

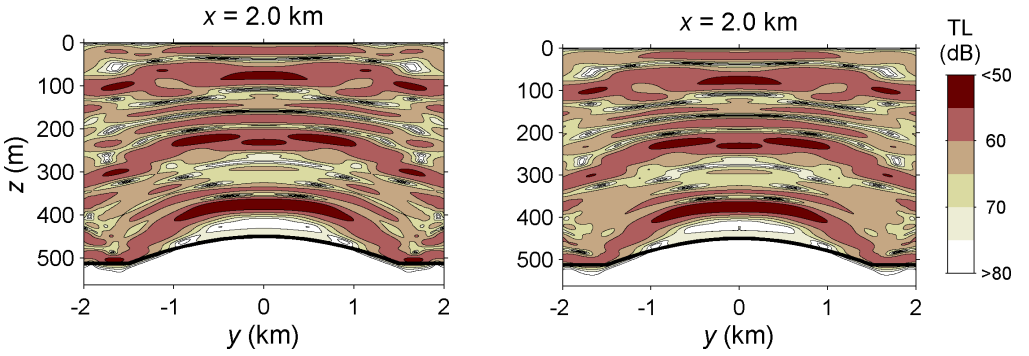

(a) 3-D cylindrical SSF PE solution $x = 2.0\,\mathrm{km}$ (b) 3-D Cartesian SSF PE solution $x = 2.0\,\mathrm{km}$

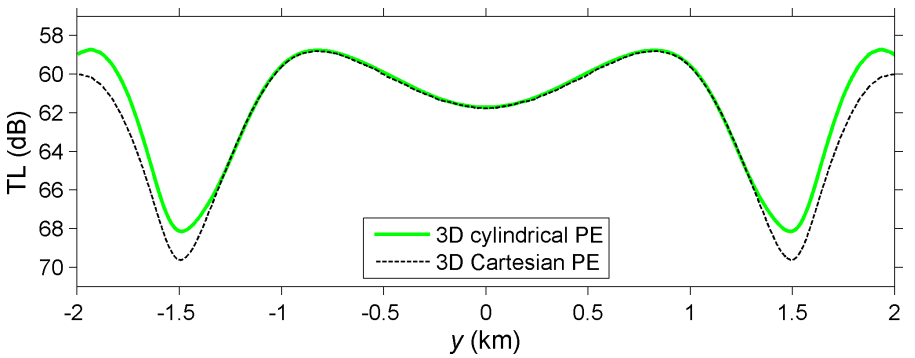

(c) Comparison of TL at 150 m depth

Fig. 7. Comparison of the TL solutions from the 3-D cylindrical and Cartesian SSF PE models. The 100-Hz sound source is placed above the tip of the seamount as shown in Fig. 5, and the TL on the y–z plane at $x = 2\,\mathrm{km}$ obtained from both the PE models is plotted in panels (a) and (b), along with the TL at 150 m depth shown in panel (c). The dark lines in panels (a) and (b) are the bathymetry.

of the TL at 250 m depth are shown in Fig. 8(c), and it shows that the two solutions start losing their agreement at a closer distance. Since the θ grid upsampling ensures the model resolution, it is producing more accurate solutions. In the next calculation, we will implement other 3-D SSF PE models to compare and confirm the θ grid upsampling scheme.

The TL solutions at 300 m depth on the horizontal x–y plane obtained from 3-D SSF PE models using cylindrical coordinates with the θ grid upsampling, arc-length coordinates and Cartesian coordinates are shown in Figs. 9(a)–9(c). The calculation setup of the Cartesian PE model follows the previous example, i.e. $\Delta x = 2\,\mathrm{m}$, $\Delta y = 1\,\mathrm{m}$, and $\Delta z = 0.5\,\mathrm{m}$. The grid sizes of the fixed arc-length model are $\Delta r = 2\,\mathrm{m}$, $\Delta s = 1\,\mathrm{m}$, and $\Delta z = 0.5\,\mathrm{m}$. All of the solutions reveal the interference patterns caused by the out-of-plane reflection of sound from the seamount bathymetry. Because of the geometric symmetry of the environment along the radial from the source to the tip of the seamount, the sound pressure field should be symmetrical, and the cylindrical models indeed produce such solutions. On the other hand, the 3-D Cartesian model fails to produce a symmetrical solution, and this is because its PE

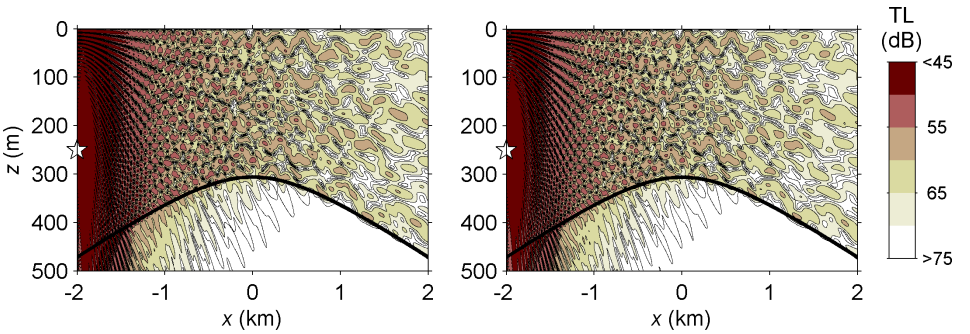

(a) 3-D cylindrical SSF PE solution (with θ grid upsampling

(b) 3-D cylindrical SSF PE without θ grid upsampling

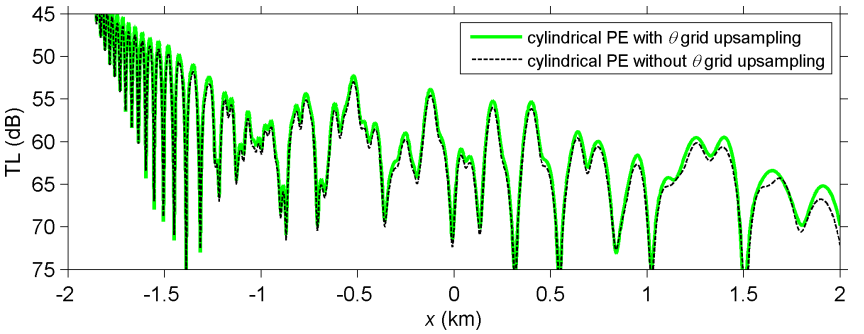

(c) TL at 250 m depth

Fig. 8. Comparison of the TL solutions from two 3-D cylindrical SSF PE models with and without θ grid upsampling. The 100-Hz sound source is placed away from the tip of the seamount as shown in Fig. 5, and the TL on the x–z plane across the source obtained from both the PE models is plotted in panels (a) and (b), along with the TL at 250 m depth shown in panel (c).

approximation error varies in azimuth away the marching direction, which is not along the line of the environmental symmetry in this case.

The PE solutions within the artificial absorbing layers imposed on the sides of the calculation domain are discarded and not plotted. However, in the cylindrical model with the θ grid upsampling, Fig. 9(a), we can still see diminishing sound intensity at the edges of the calculation domain. This is because the fixed angular aperture cannot provide large enough space in the near field for the absorbing layers to work perfectly. It should not be confused with the diminishing intensity near the source in the Cartesian model, Fig. 9(b), which is directly caused by the angular aperture of 84° given for the point source starter. The PE model using the fixed Δs grid, Fig. 9(c), indeed shows its advantage. It achieves uniform resolution in the far field, and it also provides fully 360° coverage of solution in the near field.

To evaluate the 3-D effect due to out-of-plane reflection of sound from the seamount bathymetry, we can compare the 3-D PE solutions to the N × 2D PE solution shown in Fig. 9(d). Detailed comparison of the 300-m depth TL at distance 4 km from the source

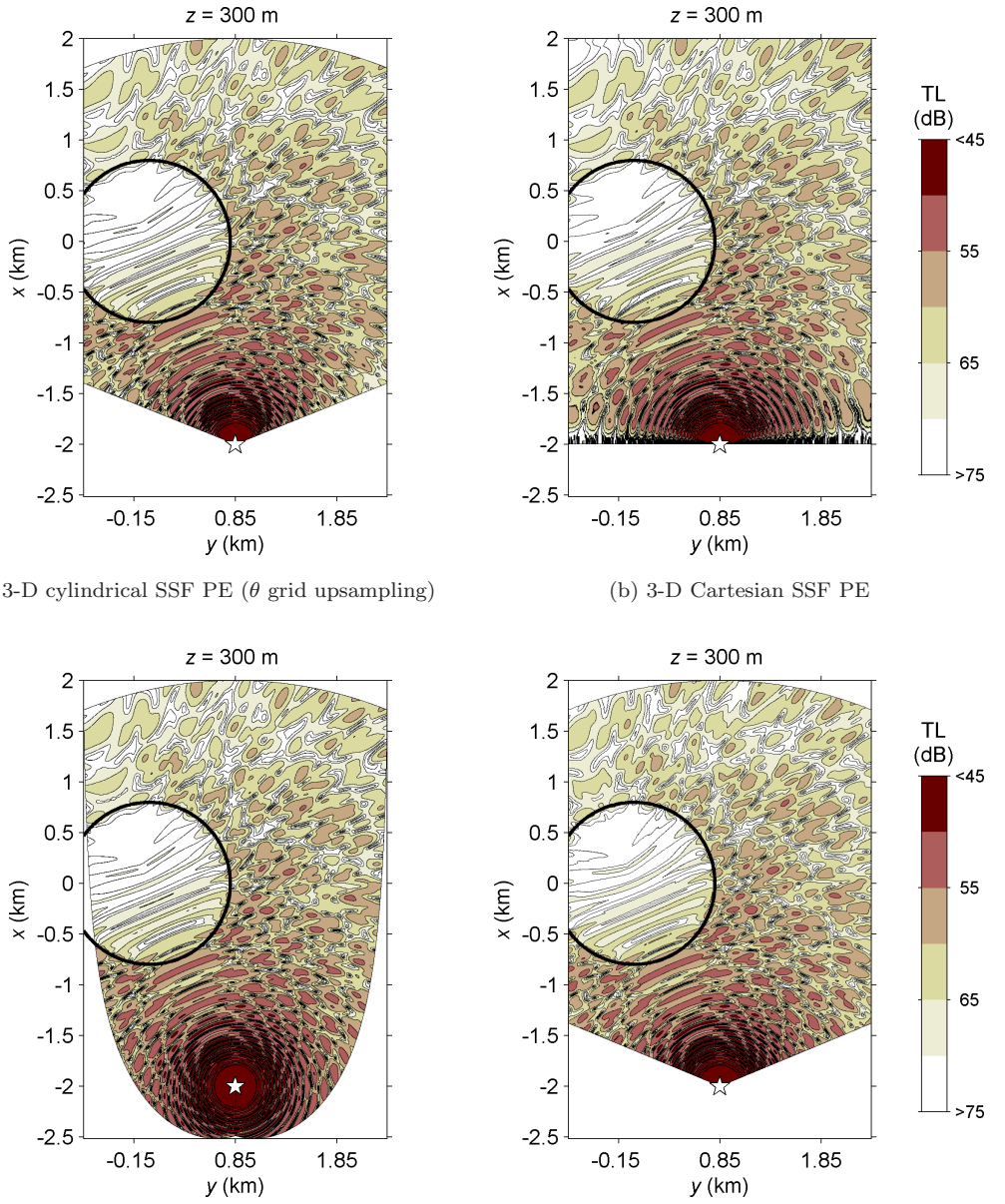

(a) 3-D cylindrical SSF PE (θ grid upsampling)

(b) 3-D Cartesian SSF PE

(c) 3-D Cylindrical SSF PE (fixed Δs grid)

(d) N × 2-D SSF PE

Fig. 9. TL solutions from four different SSF PE models. The 100-Hz sound source is placed away from the tip of the seamount as shown in Fig. 5, and the TL at 250 m depth on the x–y plane is plotted. The dark circle in each panel indicates the seamount profile at $z = 300$ m.

is shown in Fig. 10. The N × 2D solution differs from all of the 3-D solutions. The three 3-D solutions agree in this window of propagation angle ±20° from the Cartesian marching direction, with an exception at $\theta < -18°$ because the Cartesian PE does not properly model sound diffracted clockwise around the seamount.

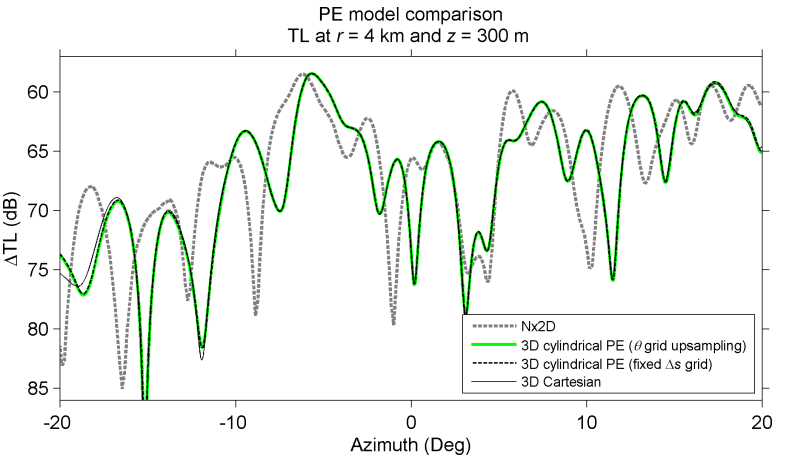

Fig. 10. Comparison of the TL solutions from the four different SSF PE models shown in Fig. 9.

4.2. *Idealized slope problem*

In this idealized slope problem we are going to test the 3-D SSF PE models in a wedge environment, as shown in Fig. 11. The model parameters of this idealized slope are explained here. The slope angle is 5°, and the medium properties in the water column and the bottom follow the idealized seamount problem presented above. The source is located 2 km away from the wedge apex at depth 100 m, and the source frequency is 75 Hz. The slope angle and the source frequency are higher than the Acoustical Society of America (ASA) wedge benchmark,[33] in order to reduce the model errors caused by the interface smoothing. Note that the width of the smoothing kernel is on the order of the acoustic wavelength, so the model errors caused by the interface smoothing are smaller for higher frequency. Also by increasing the water depth, the ratio of the smoothing width to the water depth is reduced, so the effect of interface smoothing on the pressure field solution will be suppressed.

Two 3-D SSF PE models using Cartesian and arc-length grids are implemented. In the Cartesian model, the marching step size Δx is 2.5 m (one eighth of the acoustic wavelength in the water column), the cross-range grid size Δy is 1.5 m, and the depth grid size Δz is

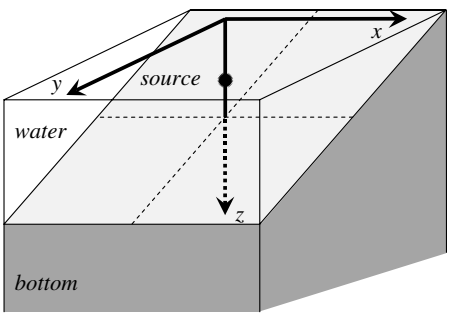

Fig. 11. Geometry of the idealized slope problem. The source frequency is 75 Hz.

1 m. In the fixed arc-length model, the marching step size Δr is also 2.5 m, the arc-length interval Δs is 1.5 m, and the depth grid size Δz is 1 m. In both models, the reference sound speed is 1475 m/s, and the one-side halfway width of the hyperbolic tangent smoothing for the water/bottom interface is set to be 5 m. The angular aperture of the wide-angle point source starter terminates at 84° with a gradual ramp-down from 82.5°.

The TL solutions on the horizontal x–y plane at $z = 30$ m obtained from both the PE models are plotted in Figs. 12(a) and 12(c). These two models agree with each other very well, except in the area of larger azimuth near the source, where the fixed arc-length

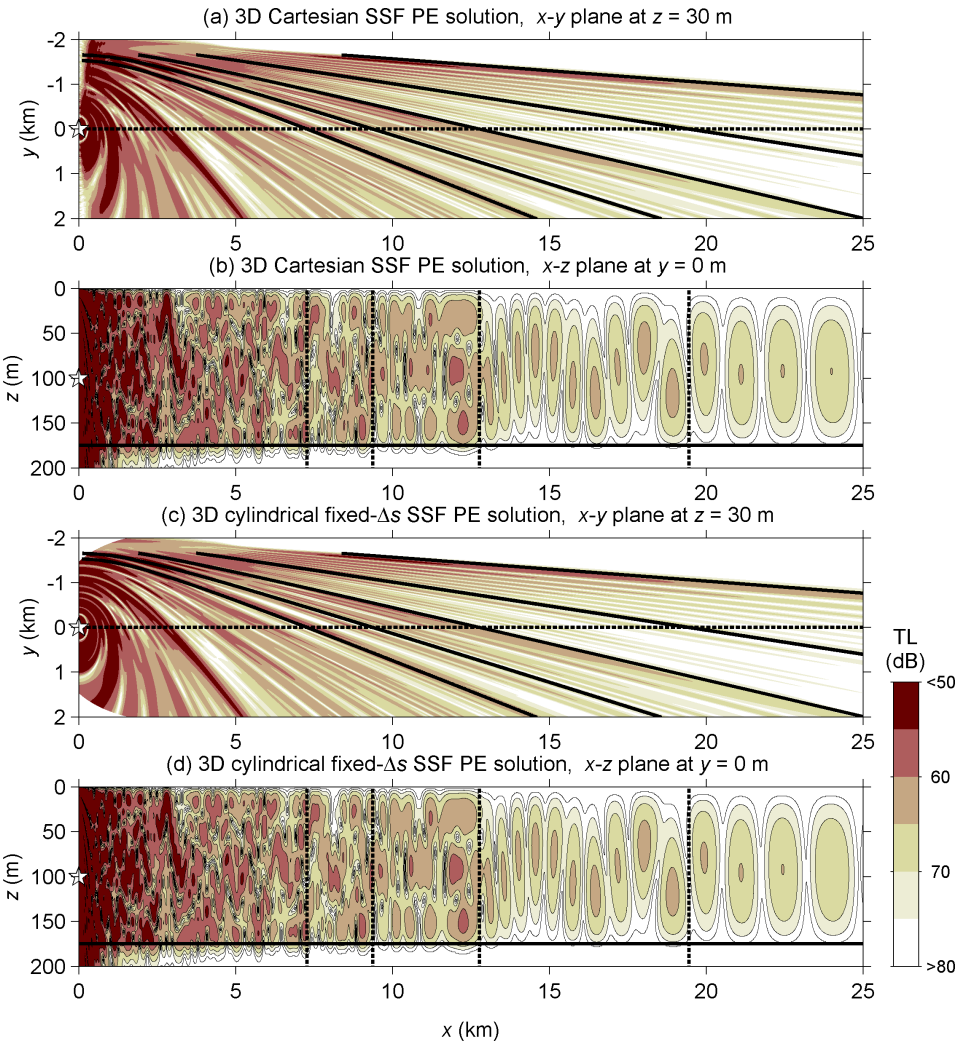

Fig. 12. The TL solutions from two SSF PE models for the idealized slope problem. The 3-D Cartesian model TL is shown in panels (a) and (b), and the 3-D cylindrical model with a fixed arc-length grid is shown in panels (c) and (d). The solid lines in panels (a) and (c) are the hyperbolic loci of the first five modal caustics predicted by Buckingham's modal theory.[34] The dashed lines in panels (b) and (d) denote the theoretical cutoff locations of modes 2–5.

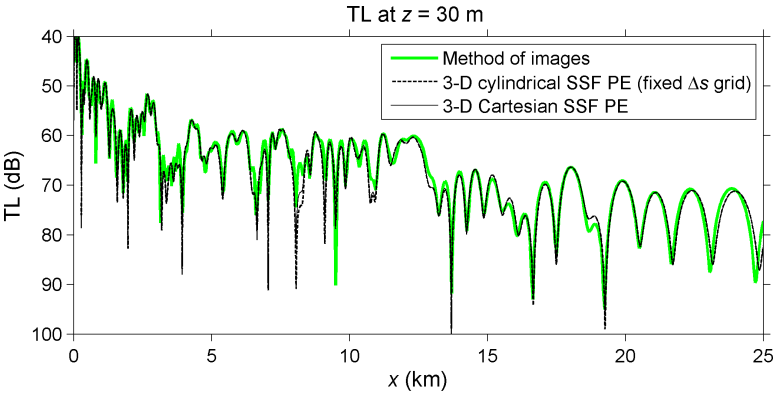

Fig. 13. Comparison of the TL solutions from three different methods.

model should outperform the other. The interference structure caused by the horizontal refraction of normal modes is clearly shown in the TL plots. Note that a given normal mode propagating across the slope will refract in the down-slope direction and form a hyperbolic caustic along the envelope of all its possible propagation paths. The caustics of modes 1–5 in this idealized slope problem are calculated using a normal mode approach proposed by Buckingham[34] and superimposed on the TL contours in Figs. 12(a) and 12(c) to examine the PE models. We can observe that the outermost border of the PE TL indeed follows the first modal caustic predicted by the Buckingham's modal approach. From the vertical interference structure shown in Figs. 12(b) and 12(d), we can confirm that the cutoff ranges of modes 2–5 at $y = 0$ seen in the PE models agree with the theoretical locations obtained from the modal caustics. An analytical solution derived from the method of images by Deane and Buckingham[17] is used here to examine the PE model TL. A total of 71 source images along a full 360° circle centered at the wedge apex are considered. Since the slope angle 5° is an integer submultiple of π in radian, there is no imaginary source image. The analytical solution involves a Bessel function expansion (see Ref. 17), and its convergence is ensured when 200 terms are included. The analytical TL solution at 30 m depth in the x–z plane at $y = 0$ is plotted in Fig. 13, and it verifies the accuracy of the PE solutions, which may still contains small but acceptable errors caused by the interface smoothing.

5. Summary

Three 3-D wide-angle split-step Fourier PE models implemented in Cartesian and cylindrical coordinate systems are presented. The performance of the models is compared. The Cartesian model is best for a plane wave-like sound field, and its numerical scheme is very efficient because its free propagation operator does not need to be updated at each marching step. The cylindrical model is suitable for a cylindrical wave-like sound field, and its numerical scheme is less efficient because the free propagation operator must be updated at each marching step. A fixed-grid Cartesian model can produce uniform model resolution

throughout the calculation domain, but a fixed-grid cylindrical model does not. Two different methods, namely angular grid upsampling and coordinate transformation from angle to arc length, are presented to achieve near-uniform resolution in the cylindrical PE model. The arc-length grid will provide solutions at all angles near the sound source because the angular aperture extends beyond 360°. However, because the arc-length gridding method does not allow use of the fast Fourier transform, it is less efficient than the other method. Thus, it may benefit the total model efficiency to switch the arc-length grid to the angular grid in the far field. The changeover is possible because both grids have cylindrical geometry.

Example calculations of sound propagation over an idealized seamount and a slope are made to verify the PE models, and reference solutions from other models are also compared to output from these models. It is found in these examples that the 3-D Cartesian PE model handles the cross-range propagation of sound extremely well within ±20° azimuthal angle measured from the PE marching direction. If a wider angular coverage is required, the improved cylindrical PE models with consistent resolution can be used with a cost of extra computational resources.

The interface smoothing required at density discontinuities for the split-step Fourier algorithm can produce model errors. A 3-D implementation of the split-step Padé algorithm,[8] which does not require interface smoothing and can handle the impedance-reduced pressure variable for conserving energy[22] across vertical interfaces, is currently under investigation.

Acknowledgments

This work was sponsored by the Office of Naval Research under the grants N00014-10-1-0040 and N00014-11-1-0701.

References

1. A. Tolstoy, 3-D propagation issues and models, *J. Comput. Acoust.* **4** (1996) 243–271.
2. F. D. Tappert, Parabolic equation method in underwater acoustics, *J. Acoust. Soc. Am.* **55** (1974) S34.
3. F. D. Tappert, Numerical solutions of the Korteweg-de Vries equation and its generalizations by the split-step Fourier method, in *Nonlinear Wave Motion*, ed. A. C. Newell, Lectures in Applied Mathematics, Vol. 15 (American Mathematical Society, New York, 1974), pp. 215–216.
4. R. H. Hardin and F. D. Tappert, Applications of the split-step Fourier method to the numerical solution of nonlinear and variable coefficient wave equations, *SIAM Rev.* **15** (1973) 423–423.
5. F. D. Tappert, The parabolic equation method, in *Wave Propagation and Underwater Acoustics*, eds. J. B. Keller and J. Papadakis, Lecture Notes in Physics, Vol. 70 (Springer-Verlag, New York, 1977), pp. 224–286.
6. D. Lee and M. H. Schultz, *Numerical Ocean Acoustic Propagation in Three Dimensions* (World Scientific Pub., Singapore, 1995).
7. D. Huang, Finite element solution to the parabolic wave equation, *J. Acoust. Soc. Am.* **84** (1988) 1405–1413.

8. M. D. Collins, A split-step Padé solution for the parabolic equation method, *J. Acoust. Soc. Am.* **93** (1993) 1736–1742.
9. F. B. Jensen, W. A. Kuperman, M. B. Porter and H. Schmidt, *Computational Ocean Acoustics*, Chap. 6 (American Institute of Physics, New York, 1994).
10. M. D. Feit and J. A. Fleck Jr., Light propagation in graded-index fibers, *Appl. Opt.* **17** (1978) 3990–3998.
11. J. M. Martin and S. M. Flatte, Simulation of point-source scintillation through three-dimensional random media, *J. Opt. Soc. Am. A* **7** (1990) 838–847.
12. T. F. Duda, Initial results from a Cartesian three-dimensional parabolic equation acoustical propagation code, Woods Hole Oceanographic Institution Technical Report, WHOI-2006-041 (2006), http://hdl.handle.net/1912/1428.
13. R. N. Baer, Propagation through a three-dimensional eddy including effects on an array, *J. Acoust. Soc. Am.* **69** (1981) 70–75.
14. K. B. Smith, A three-dimensional propagation algorithm using finite azimuthal aperture, *J. Acoust. Soc. Am.* **106** (1999) 3231–3239.
15. G. H. Brooke, D. J. Thomson and G. R. Ebbeson, PECAN: A Canadian parabolic equation model for underwater sound propagation, *J. Comput. Acoust.* **9** (2001) 69–100.
16. F. Sturm and J. A. Fawcett, On the use of higher-order azimuthal schemes in 3-D PE modeling, *J. Acoust. Soc. Am.* **113** (2003) 3134–3145.
17. G. B. Deane and M. J. Buckingham, An analysis of the three-dimensional sound field in a penetrable wedge with a stratified fluid or elastic basement, *J. Acoust. Soc. Am.* **93** (1993) 1319–1328.
18. Y.-T. Lin, A. E. Newhall, T. F. Duda and C.-F. Chen, Numerical consideration for three-dimensional sound propagation modeling: Coordinate systems and grid sizes, *10th Int. Conf. Theoretical and Computational Acoustics — Program and Book of Abstracts* (*ICTCA 2011*), 24–28 April 2011, Taipei, Taiwan, p. 36.
19. A. D. Pierce and D. Lee, The influence of the reference wavenumber in computational ocean acoustics, *J. Comput. Acoust.* **1** (1993) 77–90.
20. P. G. Bergman, The wave equation in a medium with a variable index of refraction, *J. Acoust. Soc. Am.* **17** (1946) 329–333.
21. D. Lee and S. T. McDaniel, A finite-difference treatment of interface conditions for the parabolic wave equation: The irregular interface, *J. Acoust. Soc. Am.* **73** (1983) 1441–1447.
22. M. D. Collins and E. K. Westwood, A higher-order energy-conserving parabolic equation for range-dependent ocean depth, sound speed, and density, *J. Acoust. Soc. Am.* **89** (1991) 1068–1075.
23. S. T. McDaniel, Propagation of normal mode in the parabolic approximation, *J. Acoust. Soc. Am.* **57** (1975) 307–311.
24. D. J. Thomson and N. R. Chapman, A wide-angle split-step algorithm for the parabolic equation, *J. Acoust. Soc. Am.* **74** (1983) 1848–1854.
25. L.-J. Huang and M. C. Fehler, Accuracy analysis of the split-step Fourier propagator: Implications for seismic modeling and migration, *Bull. Seismol. Soc. Am.* **88** (1998) 18–29.
26. A. R. Smith and K. B. Smith, Mode functions for the wide-angle approximation to the parabolic equation, *J. Acoust. Soc. Am.* **103** (1998) 814–821.
27. D. J. Thomson and C. S. Bohun, A wide-angle initial field for parabolic codes (A), *J. Acoust. Soc. Am.* **83** (1988) S118.
28. D. J. Thomson, Wide-angle parabolic equation solutions to two range-dependent benchmark problems, *J. Acoust. Soc. Am.* **87** (1990) 1514–1520.

29. J.-P. Berenger, A perfectly matched layer for the absorption of electromagnetic waves, *J. Comput. Phys.* **114** (1994) 185–200.
30. A. V. Oppenheim, R. W. Schafer and J. R. Buck, *Discrete-Time Signal Processing*, Chap. 4, 2nd edn. (Prentice-Hall, Inc, 1999).
31. F. Sturm and N. A. Kampanis, Accurate treatment of a general sloping interface in a finite-element 3-D narrow-angle PE model, *J. Comput. Acoust.* **15** (2007) 285–318.
32. M. E. Austin and N. R. Chapman, The use of tessellation in three-dimensional parabolic equation modeling, *J. Comput. Acoust.* **19** (2011) 221–239.
33. F. B. Jensen and C. M. Ferla, Numerical solutions of range-dependent benchmark problems in ocean acoustics, *J. Acoust. Soc. Am.* **87** (1990) 1499–1510.
34. M. J. Buckingham, Theory of three dimensional acoustic propagation in a wedgelike ocean with a penetrable bottom, *J. Acoust. Soc. Am.* **82** (1987) 198–210.